

Adaptive optics SLO/OCT for 3D imaging of human photoreceptors *in vivo*

Franz Felberer,¹ Julia-Sophie Kroisamer,^{1,2} Bernhard Baumann,¹ Stefan Zotter,¹ Ursula Schmidt-Erfurth,² Christoph K. Hitzenberger,¹ and Michael Pircher^{1,*}

¹Center for Medical Physics and Biomedical Engineering, Medical University of Vienna, Waehringerguertel 18-20, 1090 Vienna, Austria

²Department of Ophthalmology and Optometry, Medical University of Vienna, Waehringerguertel 18-20, 1090 Vienna Austria

*michael.pircher@meduniwien.ac.at

Abstract: We present a new instrument that is capable of imaging human photoreceptors in three dimensions. To achieve high lateral resolution, the system incorporates an adaptive optics system. The high axial resolution is achieved through the implementation of optical coherence tomography (OCT). The instrument records simultaneously both, scanning laser ophthalmoscope (SLO) and OCT en-face images, with a pixel to pixel correspondence. The information provided by the SLO is used to correct for transverse eye motion in post-processing. In order to correct for axial eye motion, the instrument is equipped with a high speed axial eye tracker. *In vivo* images of foveal cones as well as images recorded at an eccentricity from the fovea showing cones and rods are presented.

©2014 Optical Society of America

OCIS codes: (170.3890) Medical optics instrumentation; (110.1080) Active or adaptive optics; (170.4470) Ophthalmology; (330.5310) Vision - photoreceptors; (110.4500) Optical coherence tomography.

References and links

1. J. Z. Liang, D. R. Williams, and D. T. Miller, "Supernormal vision and high-resolution retinal imaging through adaptive optics," *J. Opt. Soc. Am. A* **14**(11), 2884–2892 (1997).
2. A. Roorda and D. R. Williams, "The arrangement of the three cone classes in the living human eye," *Nature* **397**(6719), 520–522 (1999).
3. A. Roorda, F. Romero-Borja, W. Donnelly III, H. Queener, T. J. Hebert, and M. C. W. Campbell, "Adaptive optics scanning laser ophthalmoscopy," *Opt. Express* **10**(9), 405–412 (2002).
4. D. X. Hammer, R. D. Ferguson, C. E. Bigelow, N. V. Ifimia, T. E. Ustun, and S. A. Burns, "Adaptive optics scanning laser ophthalmoscope for stabilized retinal imaging," *Opt. Express* **14**(8), 3354–3367 (2006).
5. S. A. Burns, R. Tumber, A. E. Elsner, D. Ferguson, and D. X. Hammer, "Large-field-of-view, modular, stabilized, adaptive-optics-based scanning laser ophthalmoscope," *J. Opt. Soc. Am. A* **24**(5), 1313–1326 (2007).
6. S. Ooto, M. Hangai, A. Sakamoto, A. Tsujikawa, K. Yamashiro, Y. Ojima, Y. Yamada, H. Mukai, S. Oshima, T. Inoue, and N. Yoshimura, "High-Resolution Imaging of Resolved Central Serous Chorioretinopathy Using Adaptive Optics Scanning Laser Ophthalmoscopy," *Ophthalmology* **117**(9), 1800–1809 (2010).
7. R. S. Jonnal, J. Qu, K. Thorn, and D. T. Miller, "En-face coherence gating of the retina with adaptive optics," *Invest. Ophthalmol. Vis. Sci.* **44**, U275–U275 (2003).
8. B. Hermann, E. J. Fernández, A. Unterhuber, H. Sattmann, A. F. Fercher, W. Drexler, P. M. Prieto, and P. Artal, "Adaptive-optics ultrahigh-resolution optical coherence tomography," *Opt. Lett.* **29**(18), 2142–2144 (2004).
9. R. J. Zawadzki, S. M. Jones, S. S. Olivier, M. T. Zhao, B. A. Bower, J. A. Izatt, S. Choi, S. Laut, and J. S. Werner, "Adaptive-optics optical coherence tomography for high-resolution and high-speed 3D retinal *in vivo* imaging," *Opt. Express* **13**(21), 8532–8546 (2005).
10. P. Godara, A. M. Dubis, A. Roorda, J. L. Duncan, and J. Carroll, "Adaptive Optics Retinal Imaging: Emerging Clinical Applications," *Optom. Vis. Sci.* **87**(12), 930–941 (2010).
11. A. Roorda, "Applications of Adaptive Optics Scanning Laser Ophthalmoscopy," *Optom. Vis. Sci.* **87**(4), 260–268 (2010).
12. D. T. Miller, O. P. Kocaoglu, Q. Wang, and S. Lee, "Adaptive optics and the eye (super resolution OCT)," *Eye (Lond.)* **25**(3), 321–330 (2011).
13. D. R. Williams, "Imaging single cells in the living retina," *Vision Res.* **51**(13), 1379–1396 (2011).
14. M. Lombardo, S. Serrao, N. Devaney, M. Parravano, and G. Lombardo, "Adaptive Optics Technology for High-Resolution Retinal Imaging," *Sensors (Basel)* **13**(1), 334–366 (2013).

15. M. Pircher and R. Zawadzki, "Combining adaptive optics with optical coherence tomography: Unveiling the cellular structure of the human retina in vivo," *Expert Rev. Ophthalmol.* **2**(6), 1019–1035 (2007).
16. A. Dubra and Y. Sulai, "Reflective afocal broadband adaptive optics scanning ophthalmoscope," *Biomed. Opt. Express* **2**(6), 1757–1768 (2011).
17. A. Dubra, Y. Sulai, J. L. Norris, R. F. Cooper, A. M. Dubis, D. R. Williams, and J. Carroll, "Noninvasive imaging of the human rod photoreceptor mosaic using a confocal adaptive optics scanning ophthalmoscope," *Biomed. Opt. Express* **2**(7), 1864–1876 (2011).
18. F. Felberer, J. S. Kroisamer, C. K. Hitzenberger, and M. Pircher, "Lens based adaptive optics scanning laser ophthalmoscope," *Opt. Express* **20**(16), 17297–17310 (2012).
19. W. Drexler and J. G. Fujimoto, "State-of-the-art retinal optical coherence tomography," *Prog. Retin. Eye Res.* **27**(1), 45–88 (2008).
20. M. E. J. van Velthoven, D. J. Faber, F. D. Verbraak, T. G. van Leeuwen, and M. D. de Smet, "Recent developments in optical coherence tomography for imaging the retina," *Prog. Retin. Eye Res.* **26**(1), 57–77 (2007).
21. A. G. Podoleanu and R. B. Rosen, "Combinations of techniques in imaging the retina with high resolution," *Prog. Retin. Eye Res.* **27**(4), 464–499 (2008).
22. W. Geitzenauer, C. K. Hitzenberger, and U. M. Schmidt-Erfurth, "Retinal optical coherence tomography: past, present and future perspectives," *Br. J. Ophthalmol.* **95**(2), 171–177 (2011).
23. Y. Zhang, J. T. Rha, R. S. Jonnal, and D. T. Miller, "Adaptive optics parallel spectral domain optical coherence tomography for the living retina," *Opt. Express* **13**(12), 4792–4811 (2005).
24. D. Merino, C. Dainty, A. Bradu, and A. G. Podoleanu, "Adaptive optics enhanced simultaneous en-face optical coherence tomography and scanning laser ophthalmoscopy," *Opt. Express* **14**(8), 3345–3353 (2006).
25. C. E. Bigelow, N. V. Iftimia, R. D. Ferguson, T. E. Ustun, B. Bloom, and D. X. Hammer, "Compact multimodal adaptive-optics spectral-domain optical coherence tomography instrument for retinal imaging," *J. Opt. Soc. Am. A* **24**(5), 1327–1336 (2007).
26. G. H. Shi, Y. Dai, L. Wang, Z. H. Ding, X. J. Rao, and Y. D. Zhang, "Adaptive optics optical coherence tomography for retina imaging," *Chin. Opt. Lett.* **6**, 424–425 (2008).
27. K. Kurokawa, K. Sasaki, S. Makita, M. Yamanari, B. Cense, and Y. Yasuno, "Simultaneous high-resolution retinal imaging and high-penetration choroidal imaging by one-micrometer adaptive optics optical coherence tomography," *Opt. Express* **18**(8), 8515–8527 (2010).
28. J. F. de Boer, B. Cense, B. H. Park, M. C. Pierce, G. J. Tearney, and B. E. Bouma, "Improved signal-to-noise ratio in spectral-domain compared with time-domain optical coherence tomography," *Opt. Lett.* **28**(21), 2067–2069 (2003).
29. R. Leitgeb, C. K. Hitzenberger, and A. F. Fercher, "Performance of fourier domain vs. time domain optical coherence tomography," *Opt. Express* **11**(8), 889–894 (2003).
30. R. A. Leitgeb, M. Villiger, A. H. Bachmann, L. Steinmann, and T. Lasser, "Extended focus depth for Fourier domain optical coherence microscopy," *Opt. Lett.* **31**(16), 2450–2452 (2006).
31. S. B. Stevenson and A. Roorda, "Correcting for miniature eye movements in high resolution scanning laser ophthalmoscopy," *Proc. SPIE* **5688**, 145–151 (2005).
32. R. S. Jonnal, O. P. Kocaoglu, Q. Wang, S. Lee, and D. T. Miller, "Phase-sensitive imaging of the outer retina using optical coherence tomography and adaptive optics," *Biomed. Opt. Express* **3**(1), 104–124 (2012).
33. O. P. Kocaoglu, S. Lee, R. S. Jonnal, Q. Wang, A. E. Herde, J. C. Derby, W. H. Gao, and D. T. Miller, "Imaging cone photoreceptors in three dimensions and in time using ultrahigh resolution optical coherence tomography with adaptive optics," *Biomed. Opt. Express* **2**(4), 748–763 (2011).
34. A. G. Podoleanu, G. M. Dobre, D. J. Webb, and D. A. Jackson, "Coherence imaging by use of a Newton rings sampling function," *Opt. Lett.* **21**(21), 1789–1791 (1996).
35. M. Pircher, R. J. Zawadzki, J. W. Evans, J. S. Werner, and C. K. Hitzenberger, "Simultaneous imaging of human cone mosaic with adaptive optics enhanced scanning laser ophthalmoscopy and high-speed transversal scanning optical coherence tomography," *Opt. Lett.* **33**(1), 22–24 (2008).
36. M. Pircher, E. Götzinger, and C. K. Hitzenberger, "Dynamic focus in optical coherence tomography for retinal imaging," *J. Biomed. Opt.* **11**(5), 054013 (2006).
37. M. Pircher, E. Götzinger, H. Sattmann, R. A. Leitgeb, and C. K. Hitzenberger, "In vivo investigation of human cone photoreceptors with SLO/OCT in combination with 3D motion correction on a cellular level," *Opt. Express* **18**(13), 13935–13944 (2010).
38. M. Pircher, B. Baumann, E. Götzinger, H. Sattmann, and C. K. Hitzenberger, "Simultaneous SLO/OCT imaging of the human retina with axial eye motion correction," *Opt. Express* **15**(25), 16922–16932 (2007).
39. R. G. Cucu, M. W. Hathaway, A. G. Podoleanu, and R. B. Rosen, "Variable lateral size imaging of the human retina in vivo by combined confocal/en face optical coherence tomography with closed loop OPD-locked low coherence interferometry based active axial eye motion," *Proc. SPIE* **7554**, 75540J (2010).
40. C. K. Hitzenberger, P. Trost, P. W. Lo, and Q. Y. Zhou, "Three-dimensional imaging of the human retina by high-speed optical coherence tomography," *Opt. Express* **11**(21), 2753–2761 (2003).
41. K. Wiesauer, M. Pircher, E. Götzinger, S. Bauer, R. Engelke, G. Ahrens, G. Grützner, C. K. Hitzenberger, and D. Stifter, "En-face scanning optical coherence tomography with ultra-high resolution for material investigation," *Opt. Express* **13**(3), 1015–1024 (2005).

42. M. Pircher, E. Goetzinger, R. A. Leitgeb, H. Sattmann, and C. K. Hitzenberger, "Ultrahigh resolution polarization sensitive optical coherence tomography," *Proc. SPIE* **5690**, 257–262 (2005).
43. G. J. Tearney, B. E. Bouma, and J. G. Fujimoto, "High-speed phase- and group-delay scanning with a grating-based phase control delay line," *Opt. Lett.* **22**(23), 1811–1813 (1997).
44. M. Pircher, E. Goetzinger, R. Leitgeb, and C. K. Hitzenberger, "Transversal phase resolved polarization sensitive optical coherence tomography," *Phys. Med. Biol.* **49**(7), 1257–1263 (2004).
45. C. K. Hitzenberger, "Measurement of Corneal Thickness by Low-Coherence Interferometry," *Appl. Opt.* **31**(31), 6637–6642 (1992).
46. C. K. Hitzenberger, "Optical Measurement of the Axial Eye Length by Laser Doppler Interferometry," *Invest. Ophthalmol. Vis. Sci.* **32**(3), 616–624 (1991).
47. J. I. Yellott, Jr., "Spectral Analysis of Spatial Sampling by Photoreceptors: Topological Disorder Prevents Aliasing," *Vision Res.* **22**(9), 1205–1210 (1982).
48. C. A. Curcio, K. R. Sloan, R. E. Kalina, and A. E. Hendrickson, "Human Photoreceptor Topography," *J. Comp. Neurol.* **292**(4), 497–523 (1990).
49. K. Wiesauer, M. Pircher, E. Goetzinger, C. K. Hitzenberger, R. Engelke, G. Ahrens, G. Gruetzner, and D. Stifter, "Transversal ultrahigh-resolution polarization-sensitive optical coherence tomography for strain mapping in materials," *Opt. Express* **14**(13), 5945–5953 (2006).
50. R. J. Zawadzki, B. Cense, Y. Zhang, S. S. Choi, D. T. Miller, and J. S. Werner, "Ultrahigh-resolution optical coherence tomography with monochromatic and chromatic aberration correction," *Opt. Express* **16**(11), 8126–8143 (2008).
51. E. J. Fernández, A. Unterhuber, B. Povazay, B. Hermann, P. Artal, and W. Drexler, "Chromatic aberration correction of the human eye for retinal imaging in the near infrared," *Opt. Express* **14**(13), 6213–6225 (2006).
52. R. F. Spaide and C. A. Curcio, "Anatomical Correlates to the Bands Seen in the Outer Retina by Optical Coherence Tomography: Literature Review and Model," *Retina* **31**(8), 1609–1619 (2011).
53. M. Pircher, J. S. Kroisamer, F. Felberer, H. Sattmann, E. Götzinger, and C. K. Hitzenberger, "Temporal changes of human cone photoreceptors observed in vivo with SLO/OCT," *Biomed. Opt. Express* **2**(1), 100–112 (2011).
54. J. I. W. Morgan, A. Dubra, R. Wolfe, W. H. Merigan, and D. R. Williams, "In Vivo Autofluorescence Imaging of the Human and Macaque Retinal Pigment Epithelial Cell Mosaic," *Invest. Ophthalmol. Vis. Sci.* **50**(3), 1350–1359 (2008).
55. D. Scoles, Y. N. Sulai, and A. Dubra, "In vivo dark-field imaging of the retinal pigment epithelium cell mosaic," *Biomed. Opt. Express* **4**(9), 1710–1723 (2013).
56. C. Torti, B. Povazay, B. Hofer, A. Unterhuber, J. Carroll, P. K. Ahnelt, and W. Drexler, "Adaptive optics optical coherence tomography at 120,000 depth scans/s for non-invasive cellular phenotyping of the living human retina," *Opt. Express* **17**(22), 19382–19400 (2009).
57. J. M. Enoch, "Wave-Guide Modes in Retinal Receptors," *Science* **133**, 1353–1354 (1961).
58. X. Zhu, A. Schülzgen, H. Li, H. Wei, J. V. Moloney, and N. Peyghambarian, "Coherent beam transformations using multimode waveguides," *Opt. Express* **18**(7), 7506–7520 (2010).
59. F. Felberer, G. Aschinger, J.-S. Kroisamer, C. K. Hitzenberger, and M. Pircher, "En-face adaptive optics optical coherence tomography with 3D-motion correction," *SPIE Photonics West*, San Francisco, CA (2013).
60. S. H. Lee, J. S. Werner, and R. J. Zawadzki, "Improved visualization of outer retinal morphology with aberration cancelling reflective optical design for adaptive optics - optical coherence tomography," *Biomed. Opt. Express* **4**(11), 2508–2517 (2013).
61. V. J. Srinivasan, B. K. Monson, M. Wojtkowski, R. A. Bilonick, I. Gorczynska, R. Chen, J. S. Duker, J. S. Schuman, and J. G. Fujimoto, "Characterization of outer retinal morphology with high-speed, ultrahigh-resolution optical coherence tomography," *Invest. Ophthalmol. Vis. Sci.* **49**(4), 1571–1579 (2008).
62. N. M. Putnam, D. X. Hammer, Y. H. Zhang, D. Merino, and A. Roorda, "Modeling the foveal cone mosaic imaged with adaptive optics scanning laser ophthalmoscopy," *Opt. Express* **18**(24), 24902–24916 (2010).

1. Introduction

Imaging the human retina with high resolution using optical techniques is challenging because the imaging beam has to traverse several parts of the eye. Imperfections of these optical parts of the eye induce monochromatic aberrations to the imaging beam which finally degrade resolution. In order to achieve a transverse resolution that is close to the diffraction limit, these aberrations have to be compensated for. This can be done using adaptive optics (AO), a technique known from astronomy. AO can be combined with a variety of different imaging techniques such as fundus photography [1, 2], scanning laser ophthalmoscopy (SLO) [3–6], or optical coherence tomography (OCT) [7–9]. A variety of different review papers describing different aspects and applications of the technique have been published [10–15]. One specific challenge in AO-assisted imaging, however, is resolving very small structures in the retina such as cones within the fovea (where their packing density is highest) or rods. Recent improvements in AO-SLO performance using a non planar folding of the imaging

telescopes significantly reduced monochromatic aberrations (introduced by using spherical mirrors for imaging) within an AO-SLO system and enabled for the first time a clear visualization of these small structures [16, 17]. Very recently, our group demonstrated similar results using a slightly different concept by relying entirely on lenses for imaging [18]. Although high transverse resolution has been demonstrated using AO-SLO, the axial resolution of these instruments, which depends on the numerical aperture provided by the optics of the eye itself, remains limited in comparison with OCT. OCT decouples transverse resolution from axial resolution (which depends in this case on the bandwidth of the imaging light source) and therefore provides unprecedented axial resolution in retinal images [19–22]. In order to provide isotropic resolution several groups have implemented AO into OCT systems [9, 23–27]. However, small structures such as foveal cones or rods have up to now, to the best of our knowledge not been resolved using this technology.

Because of the sensitivity advantage provided by Fourier-domain optical coherence tomography (FD-OCT) [28, 29] in comparison with time domain OCT, this technology has been mainly used in combination with AO. The sensitivity advantage results from the simultaneous recording of the entire imaging depth. However, this can also be a drawback in the case of high transverse resolution imaging because this implies a rather limited depth of focus (DOF). Therefore only a small portion of the imaged volume will be in focus and imaged sharply. To overcome this limitation either several volumes with different axial focal positions have to be recorded (which is rather time consuming) or special beams with non-Gaussian intensity distributions (e.g. by using an axicon lens [30]) have to be used. Both concepts have so far not been implemented in instruments that can be used for retinal imaging. Using higher image magnification results in an increased sensitivity to transverse eye motion artifacts. Depending on the imaging speed these artifacts will be quite pronounced in images of the retina thus heavily distorting regular structures such as the cone mosaic. While the imaging speed of AO-SLO can be sufficient in order to compensate for this motion in post-processing [31], using FD-OCT an entire volume has to be recorded to obtain en-face images which is rather slow. Recently, it has been demonstrated that by reducing the field of view and with pronounced landmarks (cones) of the underlying structure these artifacts can be significantly reduced enabling the visualization of the cone mosaic with this technique [32, 33]. However, transversal scanning (TS) (or en-face) OCT (TS-OCT) [34] might be an alternative approach for high lateral resolution imaging in combination with AO [24, 35]. The scanning protocol of TS-OCT is similar to SLO and therefore provides high transverse imaging speed. In addition TS-OCT offers the possibility of dynamic focusing, i.e. shifting the coherence gate in z-direction simultaneously with the focal plane [36]. This option alleviates the problem of the limited DOF for volume imaging and provides isotropic resolution throughout the entire volume [37]. TS-OCT is less sensitive than FD-OCT which can partly be compensated for by using higher numerical apertures and dynamic focusing. A more significant limitation of TS-OCT is the sensitivity to axial eye motion artifacts which greatly reduces the applicability of the technique. However, the implementation of an active axial eye tracking system can overcome this problem [37–39].

In this paper we present a new AO-TS-OCT instrument with active axial eye tracking. The system is based on our previously published AO-SLO system which is capable of resolving foveal cones and rods at an eccentricity from the fovea [18]. The new instrument records TS-OCT and SLO images simultaneously and the information provided by the SLO is used for transverse motion correction in post-processing. The active axial eye tracking accounts for axial eye motion. Therefore volumes with high lateral and axial resolution showing only minor residual motion artifacts can be acquired. The instrument was used to image the foveal region (where only cones are present) and a peripheral region (~8 degrees temporal to the fovea) in the retina of healthy volunteers.

2. Methods

The system is based on a Mach-Zehnder interferometer and consists of three subsystems: The TS-OCT sample arm which is based on our AO-SLO system, the TS-OCT reference arm and the axial eye tracking. The interferometer is illuminated with a superluminescence diode (SLD) operating at 840 nm with a full width at half maximum (FWHM) bandwidth of 50 nm which provides a theoretical axial resolution of ~ 4.5 μm in tissue for TS-OCT imaging. The output power of the SLD emitted from a single mode fiber was measured to be 25.9 mW. The light from the SLD is split at the entrance of the interferometer via a 90:10 fiber coupler and is launched into the two subcomponents (sample arm and reference arm) of the system. Each subsystem is described separately in the following sections.

2.1 AO-SLO/OCT sample arm

The AO-TS-OCT sample arm is similar to the AO-SLO system which has been published previously [18]. However, some modifications have been applied in order to enable TS-OCT imaging. In the following we briefly describe the key parameter of the subsystem. A scheme of the sample arm is shown in Fig. 1. Imaging is based on lenses instead of spherical mirrors and polarization optics are used in order to suppress unwanted back reflections from the telescope lenses that would otherwise influence the wavefront measurement. Scanning is performed using a Galvo scanner (GS) and a resonant scanner (RS). The RS is operated at ~ 8 kHz which yields a line rate of 16 kHz (both scanning directions are used for imaging). The AO part incorporates a deformable mirror (DM, Imagine Eyes, mirao 52-e) and a Shack Hartmann wave front sensor (SHS, Imagine Eyes, Haso 32). The AO loop is controlled via commercially available software provided by the manufacturer of the deformable mirror and SHS (Caso, Imagine Eyes). The main difference to our previously published AO-SLO setup is the implementation of an additional detection channel. The detection unit now consists of 3 parts: The SHS, the SLO detection channel, and the OCT detection channel. Thereby 20% of the light returning from the sample is used for wave front sensing, while the rest is split between the SLO (20%) and the OCT (60%) channel, respectively. Additionally, glass rods for dispersion compensation had to be inserted into the system (c.f. Fig. 1).

In order to provide a pixel to pixel correspondence between SLO and OCT channel, the light in both channels is coupled into individual single mode fibers and both fiber collimators are aligned (change of tip and tilt and lateral displacement) in SLO mode until identical images from both channels are obtained. During system operation, the light in the SLO channel is detected with an avalanche photo diode module (APD) while the light in the OCT channel is delivered to a fiber coupler at the exit of the interferometer.

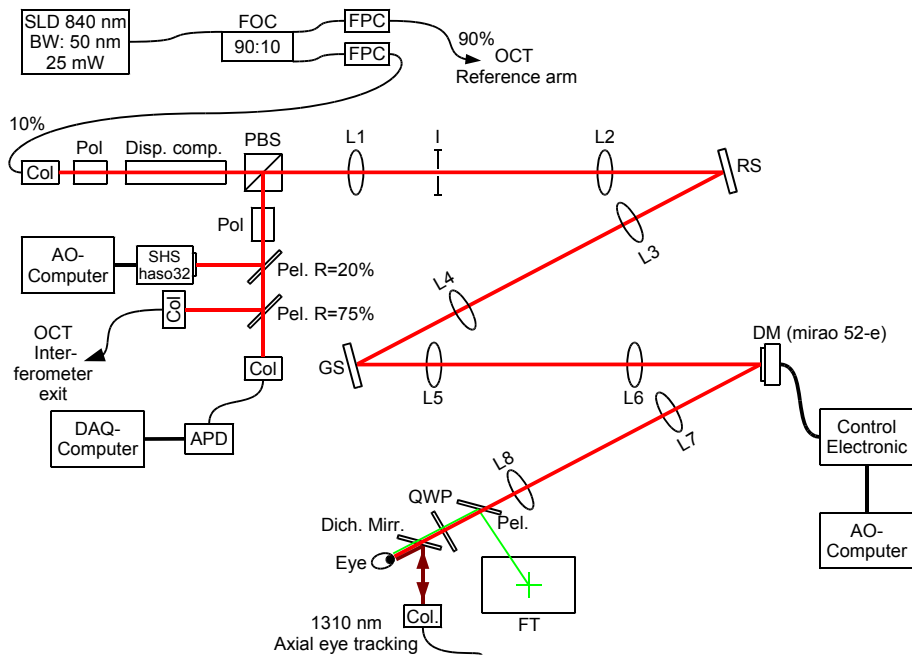


Fig. 1. Scheme of the sample arm of the AO-SLO/OCT system. SLD super luminescent diode, FOC fiber optic coupler, FPC fiber polarization controller, Col collimator, Pol polarizer, Disp. comp. dispersion compensation, PBS polarizing beam splitter, L1-L4 lenses with 200mm focal length, L5 lens ($f = 75\text{mm}$), L6 lens ($f = 250\text{mm}$), L7 lens ($f = 300\text{mm}$), L8 lens ($f = 180\text{mm}$), RS resonant scanner, GS galvanometer scanner, DM deformable mirror, Pel. Pellicle, QWP quarter wave plate, SHS Shack Hartmann wavefront sensor, APD avalanche photodiode, FT fixation target, I variable aperture stop, Dich. Mirr. dichroic mirror.

2.2 AO-SLO/OCT reference arm

A scheme of the AO-SLO/OCT reference arm and the OCT detection unit is shown in Fig. 2. The fiber coupler at the entrance of the interferometer directs 90% of the light emitted from the SLD into the reference arm. The reference arm is located on a separate optical table. Thus, an 8 m long SM-fiber is used for delivering the beam from the interferometer entrance to the reference arm. The light exiting the delivery fiber is collimated and traverses two Glan-Thompson polarizers. This ensures that the dispersion introduced by the polarizers which are placed in the sample arm is matched. Then the beam traverses two acousto optic modulators (AOM's) in order to introduce a carrier frequency for the OCT signal [40]. The use of two acousto optic modulators reduces the modulation frequency and supports a broad wavelength range [41, 42]. The (optical) frequency shifts that are applied to the beam are set to -40 MHz and $+43\text{ MHz}$, respectively which results in a net frequency shift (in comparison to the sample arm) and finally carrier frequency of the OCT signal of 3 MHz . In the case of path length matching of both arms an interference signal with the same oscillation frequency will occur. To compensate for dispersion introduced by the AOM's two glass rods of equal length and material are placed into the sample arm (c.f. to Disp. comp. in Fig. 1). The light is then directed to an optical circulator consisting of a polarizing beam splitter (PBS) and a quarter wave plate. Within the circulator the light traverses two glass rods of different length and material twice in order to compensate for the dispersion mismatch introduced by the lenses in the sample arm. Finally the light is inserted into a rapid scanning optical delay line (RSODL) [43]. The RSODL is used for a fast adaption of the reference arm length in accordance with changes in the axial position of the eye [37]. The RSODL consists of a grating, a lens and a galvanometer scanner (Cambridge Technologies). The pivot point of the GS is adjusted to

introduce only a group delay to the measurement beam [37, 43]. The beam exiting the circulator is reflected by a mirror that is mounted on a voice coil translation stage which enables independent depth scanning for the TS-OCT system. Finally, the beam is coupled into a single mode fiber. The light from the sample arm is delivered from the sample arm optical table through an 8 m long SM fiber (in order to match the dispersion of the long SM fiber used to deliver the light from the interferometer entrance to the reference arm) and is brought to interference with the light from the reference arm with a 50:50 fiber optic coupler. A balanced detector is used to detect the light emerging from both exits of the fiber coupler and the OCT signal as well as the SLO signal are recorded with a data acquisition card operating at 20 M samples per second.

In order to achieve the theoretical axial resolution that is determined by the bandwidth of the light source, the dispersion in the sample and the reference arm has to be matched exactly. However, the RSODL itself can introduce strong additional dispersion [43] if the grating is not located exactly at the focal plane of the lens. To separate this effect from dispersion mismatch in the system we replaced the grating of the RSODL with a mirror for the dispersion compensation procedure. In this procedure the length of the dispersive material was changed in one arm by using a prism pair and the coherence function obtained from a mirror was monitored. To account for dispersion which will be introduced by the eye during the measurement, a water filled, 23 mm long tube was additionally placed into the sample arm and the corresponding dispersion is compensated in the reference arm. Thus the interferometer will be balanced for the case of *in vivo* measurements (without placing a water filled tube into the reference arm). The prism pair was adjusted until a minimum of the coherence length was found. After this dispersion matching procedure the grating was re-inserted into the RSODL and the RSODL was adjusted in a way that no additional dispersion is introduced. In addition we checked the spectrum of the light returning from the reference arm (with a commercially available spectrometer) that was identical to the source spectrum.

From the bandwidth of the light source we calculated a theoretical axial resolution in air of $\sim 6 \mu\text{m}$ (assuming a Gaussian shape of the spectrum) which is in good agreement with the measured $7.3 \mu\text{m}$ in air. The OCT signal is centered at 3 MHz (carrier frequency) and we used in the detection a bandwidth of 4 MHz to account for the frequency broadening due to the transverse scanning [44]. This results, together with $60 \mu\text{W}$ power returning from the sample arm (using a mirror as sample), in a theoretical sensitivity of the system of 74 dB. However, only 70 dB was measured with this configuration. Measurements using an artificial eye consisting of a lens ($f = 30 \text{ mm}$) and a sheet of paper yielded a SNR within the image of $\sim 50 \text{ dB}$ for the OCT channel.

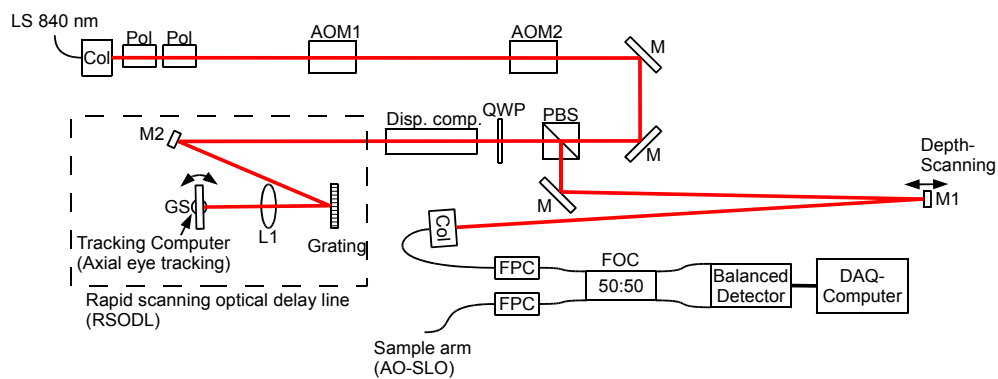


Fig. 2. Scheme of the AO-SLO/OCT reference arm. LS light source, Col collimator, Pol polarizer, AOM acousto optic modulator, M mirror, PBS polarizing beam splitter, QWP quarter wave plate, Disp. Comp. dispersion compensation, L1 lens (80 mm), GS galvanometer scanner, FPC fiber polarization controller, FOC fiber optic coupler

2.3 Axial eye tracking

The details of the axial eye tracking system are presented in [37] and a scheme of the setup is shown in Fig. 3. The system is based on a Fourier domain (FD) low coherence interferometer (LCI) operating at a center wavelength of 1300 nm. In order to combine the TS-OCT beam with the tracking beam of the FD-LCI system a dichroic mirror is used. The tracking beam is collimated which ensures that mainly light from the corneal apex is coupled back into the single mode fiber. The axial position of the cornea is measured (with an accuracy that is better than the coherence length of the light source [45]) and is used to change accordingly the reference arm length of the TS-OCT system via the galvanometer scanner in the RSODL. In order to operate the axial eye tracking at high speed which is necessary for reducing axial eye motion artifacts, data evaluation and galvanometer scanner driving signal generation are performed with a real time system (National Instruments, LABVIEW Real-time).

With the axial eye tracking system the axial position of the eye can be monitored with high precision. This allows the alignment of the eye during measurement in order to place the pupil plane of the eye in the focal plane of the last lens (c.f. L8 in Fig. 1) of the AO-TS-OCT sample arm. Prior to the measurement the distance can simply be adjusted with the reference arm length of the FD-LCI instrument. This alignment ensures that the pivot points of the scanners are imaged onto the pupil plane of the eye.

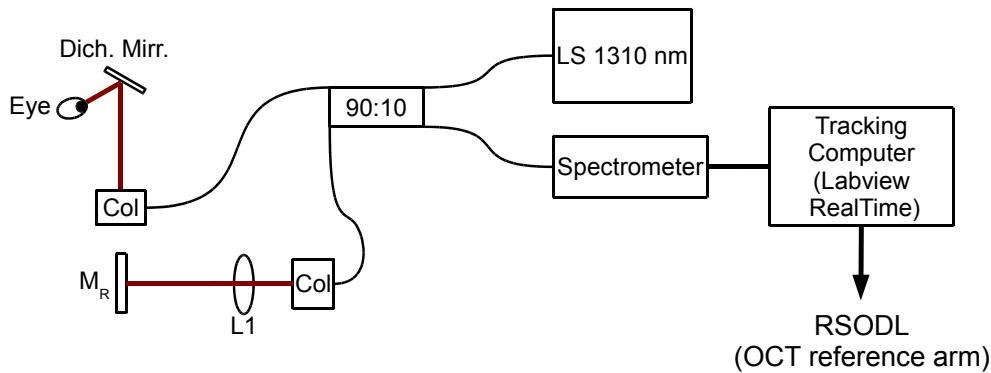


Fig. 3. Scheme of the axial eye tracking system. LS light source, Col Collimator, L1 lens, Dich. Mirr. dichroic mirror.

3. Scanning protocol and post processing

In order to evaluate the performance of the instrument, measurements were taken from 3 healthy volunteers (mean age 34 years). Prior to imaging informed consent was obtained after the nature and possible risks of the measurement had been explained. The evaluation was performed under a protocol that was approved by the local ethics committee (Medical University of Vienna) and which adhered to the tenets of the Declaration of Helsinki. The power at the cornea of the eye for the 840nm imaging beam is kept well below 700 μW to meet the requirements for safe illumination of the eye given in the laser safety standards [39].

A scan angle of 1x1 degree with a frame rate of 20 frames per second was used. Each frame consists of 1152 (x) times 790 (y) pixels. Thereby both scanning directions (forward and backward scan) of the 8 kHz resonant scanner were used to record the data. The scanning depth (z) was set to 200 μm (optical) and a volume scan took 6 sec resulting in a total of 120 recorded frames. The signal in both channels (SLO and OCT) is sampled with a data acquisition card operating at 20M samples per second. The adaptive optics correction is performed in closed loop with a bandwidth of 10 Hz and is kept operating during the measurements.

Imaging was performed with an artificially dilated pupil, unless the natural pupil size of the volunteer in the dark measurement environment already exceeded 7 mm. The pupil

diameter was measured with the SHS, However no drugs were used to prevent accommodation. The head was positioned in a way to ensure that the pupil of the eye was imaged centrally on the SHS. In a next step the axial position of the eye was adjusted in order to fit into the center of the measurement range of the axial eye tracking system. The AO loop and the active axial eye tracking were activated and the length of the reference arm was adjusted by shifting the depth scanning mirror (M1 in Fig. 2) in order to account for the individual eye length. The correct length was found when the junction between inner and outer segments of photoreceptors (IS/OS) became visible in the en-face OCT image. When starting a volume scan acquisition, the reference arm length was slightly increased (corresponding to a location of $\sim 50 \mu\text{m}$ deeper into the tissue) prior to the measurement. During data recording the length was then continuously reduced up to a total length change of $200 \mu\text{m}$ corresponding to a shift of the coherence gate from posterior to anterior layers.

The OCT and SLO signals were recorded simultaneously and have a pixel to pixel correspondence. The depth resolution of the SLO was on the order of $50 \mu\text{m}$. Therefore with SLO always the same image was recorded regardless of the imaging depth of the recorded OCT en-face images which can be used for transverse eye motion correction. We followed a similar approach as is used for AO-SLO imaging to correct for transverse motion [31] and applied all post-processing steps for motion correction on both channels. These steps incorporated correction for the sinusoidal scanning velocity of the RS, correction for transverse motion using cross correlation on the entire image and finally, correction of in-frame distortions by registering each image strip-wise to a manually chosen reference frame. This procedure ensures that all OCT en-face images are transversally registered to each other with an accuracy that is better than the extension of a single cone. For recalculating from scanning angle into distances on the retina, we measured the eye length of the volunteer by a partial coherence interferometer [46] using a commercially available instrument (Carl Zeiss Meditec, IOLMaster).

4. Results

Figure 4 shows images recorded at the foveal region of a healthy volunteer with the new instrument. In order to compare both imaging modalities, averaged SLO (120 frames) and depth integrated OCT images (70 frames) are displayed in 4(a) and 4(b). The cone mosaic is clearly visible throughout both images. However, cones appear less clear in the central $50 \mu\text{m}$ (indicated with a white square in the Fig. 4(a) and 4(b) and displayed enlarged in Fig. 4(c) and 4(d)). Therefore we calculated FFT's from this central region (c.f. Fig. 4(e) and 4(f)) where Yellott's ring [47] can be clearly observed, indicating the regular arrangement of the cones in this area and demonstrating the high lateral resolution of the instrument. In addition we calculated a radial average of Fig. 4(e) in order to measure the row to row spacing between the cones in the fovea. The result is shown in Fig. 5 and Yellott's ring appears at the location of $0.366 \text{ cycles}/\mu\text{m}$. This corresponds to a next neighbor spacing (assuming a hexagonal packing of the cones and multiplication by $1/\cos 30^\circ$ as conversion factor) within the fovea of $\sim 3.11 \mu\text{m}$ which is in good agreement with results obtained from histology [48].

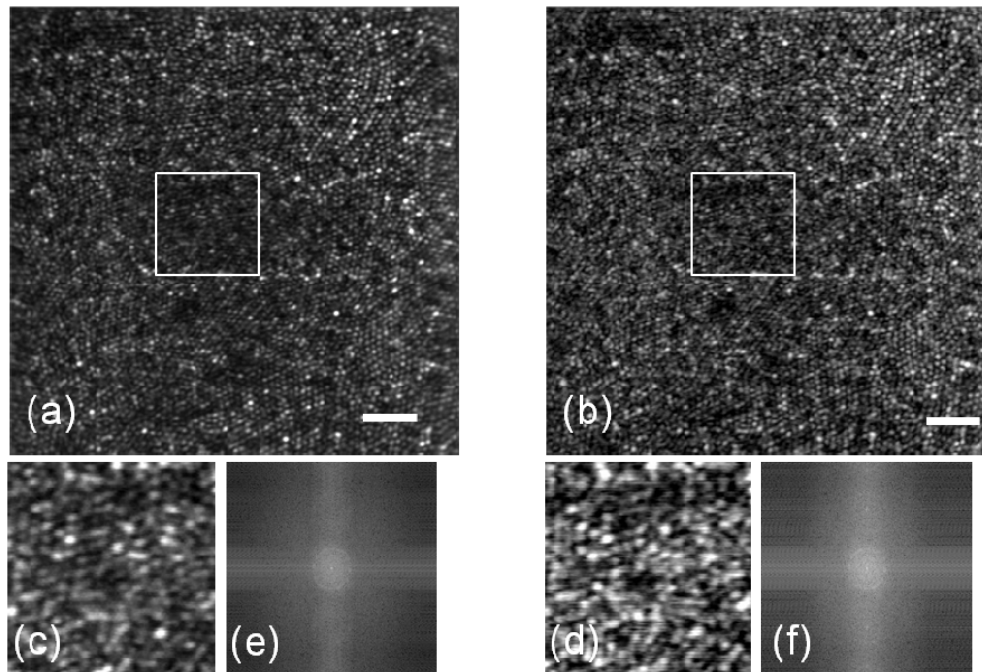


Fig. 4. Averaged en-face SLO image (a) and depth integrated and squared OCT image (b) of the fovea of subject 1. (Both image channels are acquired simultaneously). The position of the center of the fovea (peak cone density) lies within the white square. (c) and (d) show an enlarged view of this central region (indicated with the white square in (a) and (b)). (e) and (f) show Yellott's ring after FFT's of (c) and (d). The scale bar is $30\mu\text{m}$.

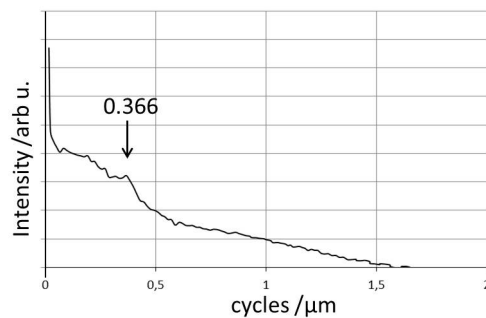


Fig. 5. Radial average of Fig. 4(e) indicating the frequency of Yellott's ring (marked with an arrow).

[Media 1](#) shows a fly through movie of the entire OCT volume scan. The depth resolution provided by OCT allows for segmentation (based on different depth locations) of individual layers of the retina. Figure 6 shows some segmented layers identified as the external limiting membrane (ELM), the junction between inner and outer segments of photoreceptors (IS/OS), the cone outer segments (OS), the end or posterior tips of photoreceptors (ETP), and the retinal pigment epithelium (RPE). The cone mosaic can only be observed within the IS/OS and the ETP layers.

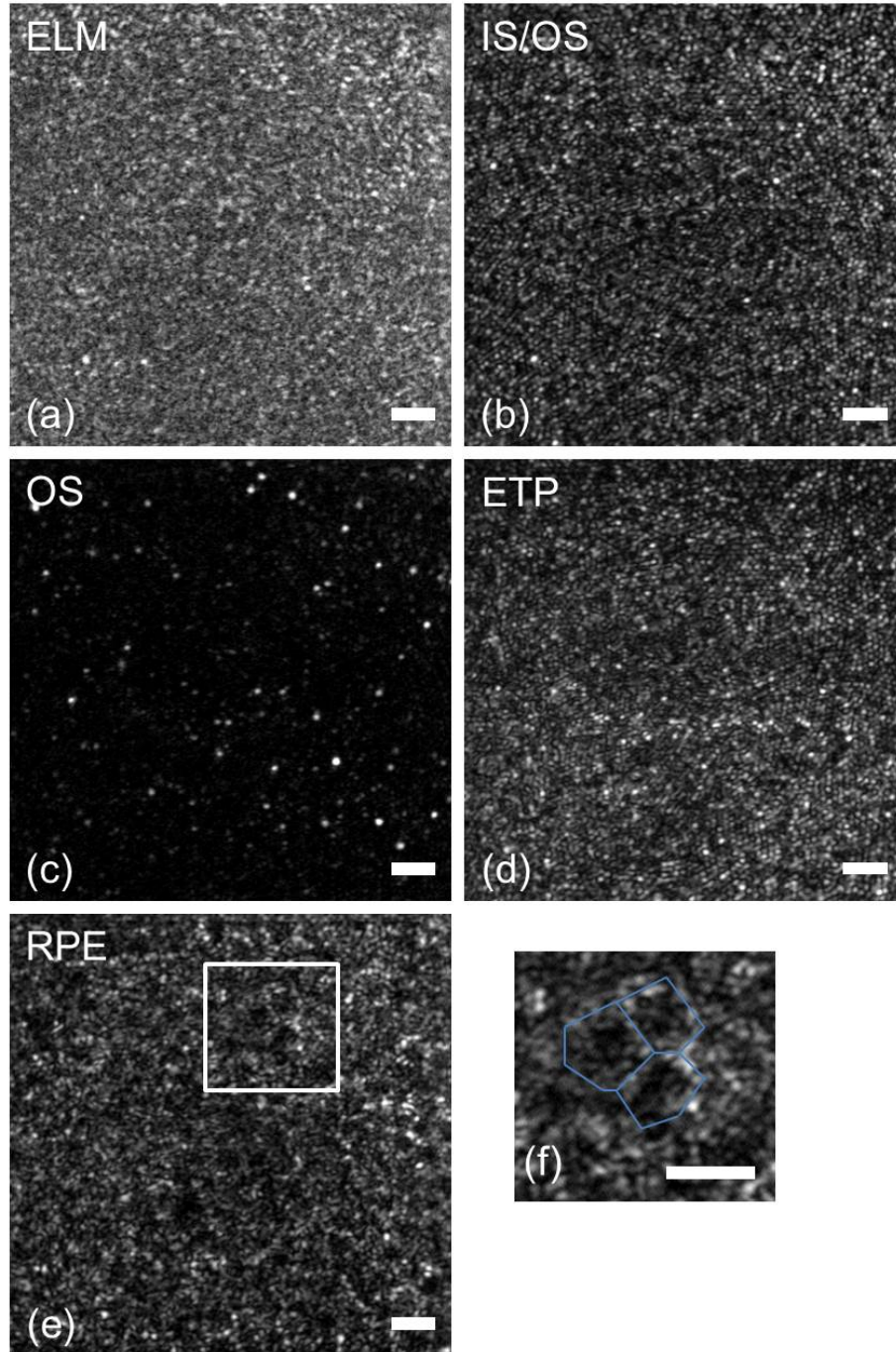


Fig. 6. Depth averaged en-face images of the center of the fovea (subject 1) retrieved from the volume scan ([Media 1](#)) of the external limiting membrane (ELM, 26 μm depth averaged) (a), the junction between inner and outer segments of photoreceptors (IS/OS, 22 μm depth averaged) (b), the outer segments (OS, 17 μm depth averaged) (c), the end tips of the cones photoreceptors (ETP, 20 μm depth averaged) (d), and retinal pigment epithelium (RPE, 15 μm depth averaged showing a regular structure) (e). (f) Enlarged section indicated by the white square in (e). The borders of the regular structure are emphasized with the blue lines. The scale bar in the images is 30 μm .

Media 2 (Fig. 7) shows a fly through movie of B scans extracted from the recorded volume. Although depth scanning was performed relatively slow (~6 sec.) the axial eye tracking greatly reduced axial eye motion artifacts and individual cone photoreceptors can be resolved throughout the images. Although the separation between the ETP layer and the RPE is not very clear in these images distinct pairs of reflections within the ETP and IS/OS layer can be observed. Figure 8 shows selected regions of interest of the 3D data set. The signal from the ELM is in general rather weak. However, in some regions where a signal can be observed the ELM reveals a similar structure as the IS/OS and ETP layer (c.f. Fig. 8(a)). At some locations photoreceptors show an OCT signal throughout their outer segment (c.f. Fig. 8(b)). Figure 8(c) shows a typical bright reflection spot within the outer segment. Interestingly, one photoreceptor shows a pronounced displacement of the IS/OS signal to the anterior layers together with a bright reflection spot in the outer segment (c.f. Fig. 8(d)).

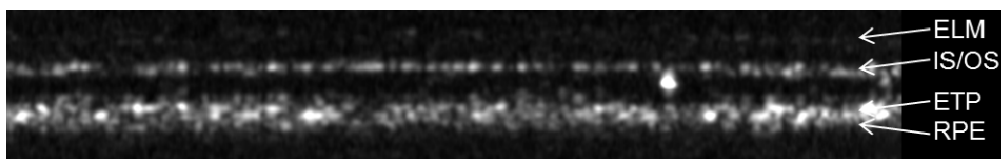


Fig. 7. Center frame of a B-scan fly through movie (**Media 2**) of the recorded volume from the fovea region of subject 1 (image size: $\sim 0.8^\circ \times 200\mu\text{m}$).

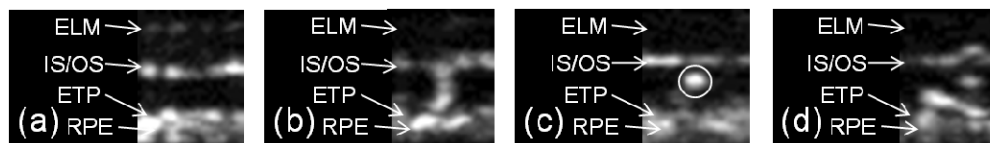


Fig. 8. Selected regions of interest of the data set shown in **Media 2** (subject 1). (a) cones showing distinct signals from three layers: ELM, IS/OS and ETP, (b) cone showing a signal throughout the outer segment, (c) Bright reflection spot (encircled) within the outer segment, (d) cone with signal from the IS/OS junction anterior to the IS/OS junction of neighboring cones.

In a next step we investigated the capability of the system to image rod photoreceptors. For this purpose we chose a location of approximately 8 degrees temporal to the fovea for imaging. Figure 9 shows the averaged SLO and depth integrated en-face OCT images, respectively. The SLO image appears similar to previously published results using AO-SLO [17, 18]. The larger and sparsely packed cones (bright spots) are surrounded by smaller and densely packed rods (small and dimmer spots). Although the rod mosaic cannot be observed throughout the entire image, at some locations individual rods can be identified. We measured the nearest neighbor distances of 5 to 10 rods in these regions and found a mean distance of $\sim 2.2\ \mu\text{m}$ which corresponds well with the next neighbor distances observed in histology or AO-SLO [17, 48]. **Media 3** shows an en-face fly through of the whole scan volume.

In Fig. 9(b)-9(f) depth segmented images corresponding to individual layers of the retina are shown. The first layer that was extracted was the external limiting membrane (Fig. 9(b)). This layer provides only a very weak backscattering signal and in our images no regular structure can be observed. Moving the imaging plane deeper into tissue, to the location of the IS/OS junction, reveals a regular pattern (c.f. Fig. 9(c)). At this junction, both photoreceptor types (rods and cones) are expected to contribute to the OCT signal. However, backscattering from cones is much stronger than from the rods and the signal from the cones is therefore dominating [17]. Interestingly, many cones show an irregular intensity distribution (e.g. doughnut like or double spot). Images recorded with AO-SLO already showed a non-homogenous backscattering signal from these large cones [17], however, all layers (RPE, ETP rods, ETP cones and IS/OS junction) contribute to the AO-SLO signal, distorting the pattern visible in Fig. 9(c). When the coherence plane is moved further posterior to the

location of the end tips of cones we observe isolated bright spots that resemble the cone mosaic (c.f. Fig. 9(d)). Only few cones in this layer show irregular intensity patterns. Moving the coherence plane slightly posterior ($\sim 14 \mu\text{m}$), a completely different structure becomes visible (c.f. Fig. 9(e)). This structure consists of large dark patches that are surrounded by a brighter structure. A comparison of this image with Fig. 9(a) shows that the locations of the large dark patches correspond to the locations of the cones, while the location of the brighter structure lies in between the cones. In the RPE (c.f. Fig. 9(f)) no regular structure (e.g. RPE cells) can be observed. [Media 4](#) shows a fly through movie of B scans extracted from the recorded volume. The irregular shaped signal originating from the cones can also be observed in these B-scans. Figure 10 shows an exemplary B-scan image from this data set and an average over all B-scans in [Media 4](#). The separation between RPE and the anterior layer (located between ET cones and RPE) is very weak and can only faintly be recognized within the averaged B-scan.

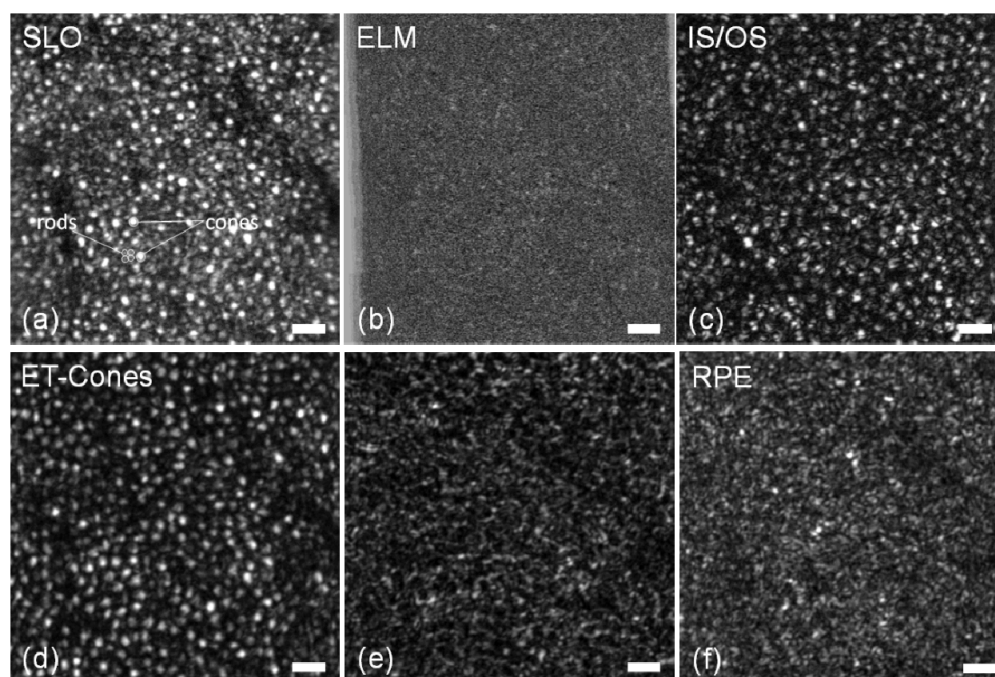


Fig. 9. SLO/OCT images recorded at $\sim 8^\circ$ eccentricity from the fovea of subject 2. Averaged SLO image (120 frames) (a), depth averaged en-face images of the external limiting membrane (b), junction between inner and outer segments of photoreceptors (c), end tips of the cones (d), layer between ET cones and RPE (e), and of the retinal pigment epithelium (f). The scale bar in all images is $30 \mu\text{m}$. [Media 3](#) shows the entire volume scan.

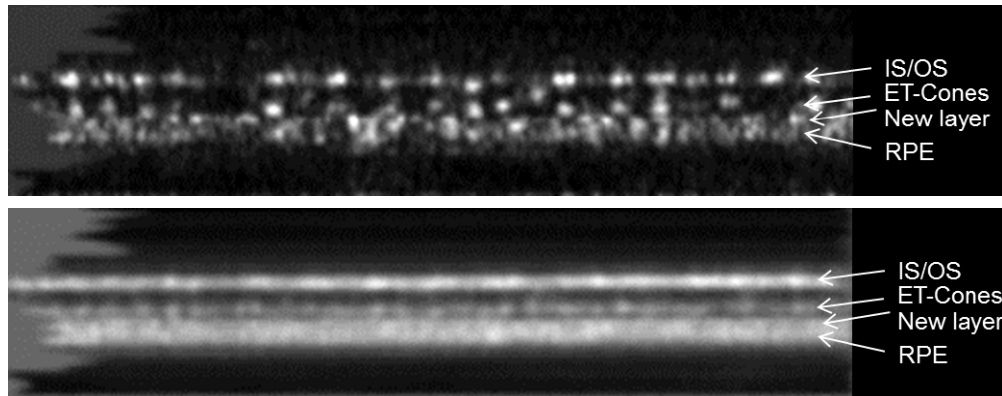


Fig. 10. Representative B-Scan taken from the volume scan (Media 4) recorded in subject 2 at ~8 degree temporal to the fovea (top). Average over all B-scans (bottom). (Images are displayed on a linear grey scale, image size: 0.8° (x) x $200\mu\text{m}$ (z)). The light grey part on the left part of the image is caused by missing data due to eye motion.

One advantage of the new AO-OCT system is the ability to record several en-face images at a certain depth within the retina. Thereby, the active axial eye tracking ensures that exactly the same imaging depth is recorded. This enables an improvement of the signal to noise ratio for a specific layer in a similar way as is done in AO-SLO imaging. Media 5 shows a movie of OCT images recorded while the imaging depth of the OCT channel was kept at a position that corresponds to the new layer located between the end tips of cone photoreceptors and RPE. Image frames that showed severe motion artifacts (e.g. micro saccades) were removed from the data set. The residual tracking error is well below the depth resolution of the system, therefore the same imaging depth can be observed throughout the image sequence. In Fig. 11 the corresponding averaged SLO and OCT images are displayed. In order to better visualize the complementary information provided by OCT, Fig. 12 shows composite false color images of the layers ETP cones and the new layer that is located between RPE and ETP cones. Both layers were recorded sequentially within the same imaging session.

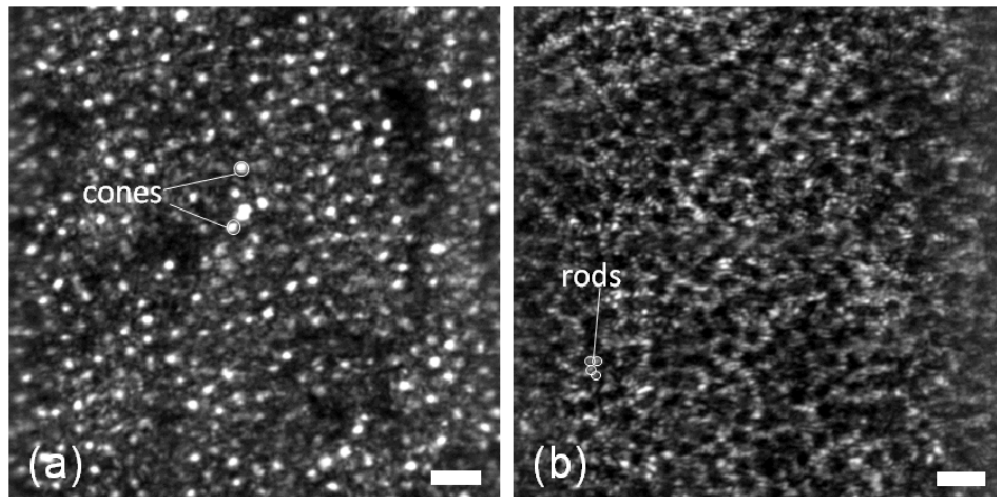


Fig. 11. Averaged (40 frames) en-face SLO image (a) and averaged OCT image (b) (recorded at an imaging depth corresponding to the layer between RPE and end tips of cones) retrieved from the volume scan shown in Media 5 of the retina (subject 2) recorded approximately 8 degree temporal from the fovea. The scale bar is $30\mu\text{m}$ (Media 5 is best viewed in loop mode).

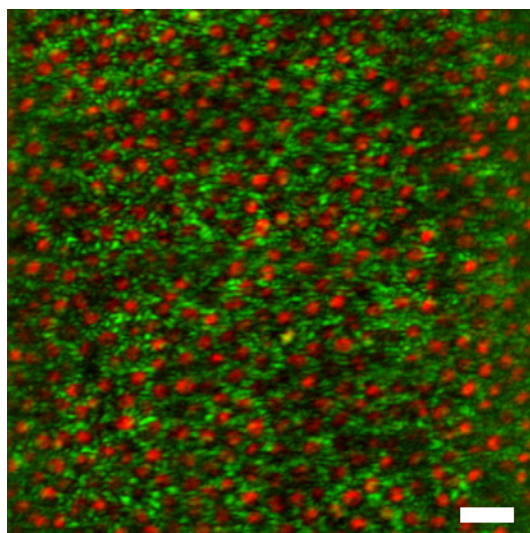


Fig. 12. Composite false color image of different retinal layers of subject 2. End tips of cones (red), and layer located between end tips of cones and RPE (green) and (scale bar: 30 μ m).

5. Discussion and conclusion

We presented a new AO-SLO/OCT instrument providing high lateral and axial resolution. Eye motion artifacts, a limiting factor for high resolution imaging systems, are largely reduced using a high speed axial eye tracker together with transverse motion correction in post processing. Currently, the axial resolution is limited to ~ 5 μ m in tissue by the light source. In order to improve the axial resolution a light source with a larger bandwidth has to be used. Thereby the AOM modulated en-face OCT technique is not a limiting factor as we could demonstrate with previous systems that achieved an axial resolution of 1-2 μ m [49]. However, power losses within the system are rather high which requires the implementation of powerful light sources such as titanium sapphire lasers. In addition a larger spectral bandwidth will put higher demands on the AO-correction as chromatic aberrations of the eye (longitudinal and transverse) have to be compensated for. Longitudinal chromatic aberrations may be compensated for using an achromatizing lens [50, 51].

An unsolved issue of the instrument is the slight discrepancy (~ 4 dB) between theoretically expected and measured sensitivity. Although we varied the power returning from the reference arm, we were not able to reach the shot noise limit. Probably the implementation of detectors with better noise characteristics may solve this issue. Nevertheless the sensitivity of the instrument was sufficient to image the cone and rod photoreceptors in healthy volunteers because of the high collection efficiency provided by the high numerical aperture and the AO correction.

The fovea is the most important region for normal daylight vision. The visualization of individual cone photoreceptors in the fovea might therefore be an important tool for clinicians to detect early onsets of a disease (e.g. age related macular degeneration). The depth resolution provided by OCT enables a clear separation between the layers which may simplify interpretation of these images. In this context it should be mentioned that the nomenclature of the outer retinal layers (IS/OS and end tips) in OCT images within the literature is to some extent controversial [52]. We therefore decided to keep our previously used nomenclature. A detailed analysis requires an accurate comparison of our data with anatomical data and is beyond the scope of this paper.

In the following we discuss some of our observations of imaging posterior retinal layers in more detail. In Fig. 6(b) and 6(d)) (corresponding to the IS/OS and ETP layers) the same

cones can be seen although the appearance of the mosaic is slightly different. This may be caused by a differing reflectivity of the individual cones at both layers. It has been shown for cones at an eccentricity from the fovea that their reflectivity changes over time in both layers [32, 53]. This effect is probably caused by the renewal process of the outer segments of cones. Within the outer segments of cones (c.f. Fig. 6(c)) bright reflection spots (BRS) can be observed [37]. In a previous study we could show that some BRS are changing their depth location with time according to the renewal process of the outer segments [53]. We hypothesized that the origin of these BRS might be defects within the packing arrangement of the outer segment discs.

Interestingly, at the level of the RPE (c.f. Fig. 6(f)) a regular structure can be observed. In order to emphasize regular arrangements within the images we performed FFT's over the entire field of view for all images in Fig. 6. The result is displayed in Fig. 13. Three layers show Yellott's ring. The outer two photoreceptor layers (IS/OS and ETP) and the RPE. In order to quantify the spacing of the structure we performed a radial average over the images in Fig. 13. The result is shown in Fig. 14. Note that the spatial frequency within the RPE layer is much lower than within the photoreceptor layer. Although the pattern is not as clear as images from RPE cells obtained with AO assisted fluorescence methods [54] or dark field SLO detection schemes [55], the arrangement and size of the structure suggest that it may be associated with individual RPE cells. Faintly, a second, larger ring can be observed in Fig. 13(e) which indicates a residual influence of the signal originating at the ETP layer to the signal observed from the RPE layer (an improvement in depth resolution might solve this issue).

It should be noted, however, that we observed this pattern only in the images of one healthy volunteer. In the other volunteers we could not detect a regular structure within the RPE (these images appear similar to the RPE shown in Fig. 9(f)). A similar visualization has been presented some years ago using AO-FD-OCT [56].

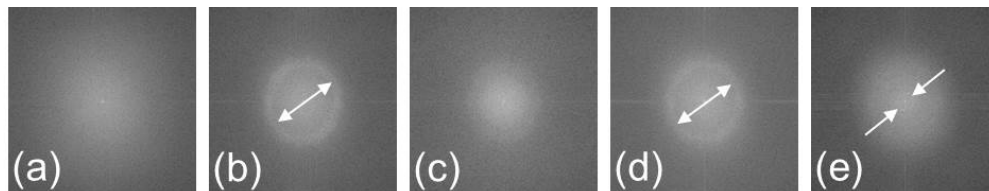


Fig. 13. FFT's over the entire field of view of the individual retinal layers displayed in Fig. 6. (a) external limiting membrane (ELM), (b) the junction between inner and outer segments of photoreceptors (IS/OS), (c) the outer segments (OS), (d) the end tips of the cone photoreceptors (ETP), and (e) retinal pigment epithelium (RPE) (Yellott's rings are indicated with white arrows).

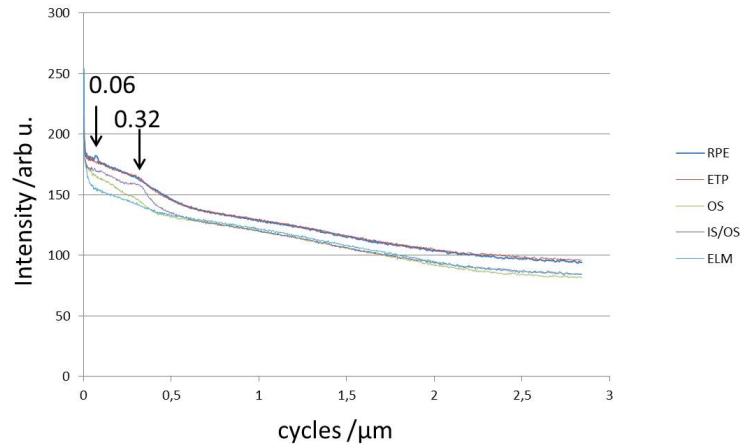


Fig. 14. Radial average of the images displayed in Fig. 13 indicating the frequency of Yellott's rings (The location of the ring from the RPE and IS/OS are marked with an arrow and the corresponding frequency value that was determined manually is displayed)

At an eccentricity of $\sim 8^\circ$ from the fovea the separation in depth provided by the AO-SLO/OCT instrument enables the visualization of different reflection sites (IS/OS and ETP) within the cone photoreceptor layer that have a different appearance. While the IS/OS layer shows an irregular pattern, the ETP layer shows distinct and regular arranged bright spots. The irregular pattern observed at the IS/OS layer may be caused by the wave guiding properties of the cones. Wave guiding can result, depending on the wavelength and the diameter of the waveguide, in different propagation modes [57]. The regular pattern observed at the ETP might be caused by the smaller diameter of cones at this location (cones are getting smaller in diameter towards the posterior tips). On the other hand a signal originating from the rod photoreceptors at the IS/OS layer may additionally contribute to the irregular pattern. (At the location of the ETP layer no signal at the location of the rods can be observed.) The shape of a propagation mode depends on the wavelength and on the underlying waveguide structure [58] which might therefore be used to obtain additional information on the cone structure. In addition it raises questions about the light field exiting these cones which may influence the appearance of images recorded from deeper retinal layers (e.g. RPE).

An interesting observation is the new layer which is located between the end tips of cones and the RPE (c.f. Figure 9(e) and 11(b)). This observation was presented at Photonics West 2013 [59] and in a paper that was published during the preparation of this manuscript [60]. This layer shows a structure that completely differs from the ETP and the RPE layers. We propose that this layer can be associated with the end tips of rods because of the following reasons. A signal from this layer is only visible at locations where no cones are present but rods (which are known to surround cones). The signal from this layer consists of very small dots and the spacing of these dots corresponds to the spacing of rods. In addition the signal strength from these dots clearly dominates over the signal strength observed in between the cones from anterior layers (c.f. Figure 9(b), 9(c), 9(d)). Therefore the main contribution to an SLO signal at the location of the rods will be from this layer. Finally, as is known from histology [49], the outer segment lengths of rods are slightly longer than the OS lengths of cones. At large eccentricities this separation has been visualized in OCT B-scans with ultrahigh resolution OCT [61]. Although the depth separation in the B-scan is not as clear as in the ultrahigh resolution images, the completely different appearance in the en-face imaging plane indicates the presence of an additional layer. With our new system the rod photoreceptor mosaic, as has been shown with AO-SLO [17], cannot be resolved in the entire image. There are differences between our system and the AO-SLO presented in [17] which

may explain the poorer visibility of the rod mosaic in our images. First, our system is operated at a longer wavelength region (840 nm vs. 680 nm and 775 nm). Therefore the theoretical resolution of our system is lower. Second, we did not perform averaging of data over an extended period of time which further helps visualizing the rod mosaic [17]. Third, the spectral bandwidth of our light source is much larger (in order to achieve high axial resolution with OCT) which may influence the lateral resolution (e.g. by chromatic aberration). Fourth, OCT is a coherent imaging technique which may result in lateral coherent effects as described in [62].

However some locations clearly show individual rod photoreceptors. This further strengthens our above mentioned association of this layer with the end tips of rods. The question remains if others parts of the retina (e.g. extensions of the RPE that surround individual cones) may mimic a similar signal. However, in this case the same structure should be observed using AO-SLO because, as mentioned above, the anterior photoreceptor layers show only a weak backscattering signal at these locations.

One advantage of the en-face OCT system over conventional (FD) OCT instruments is the high en-face imaging speed. Together with the axial eye tracking a specific layer at a certain imaging depth can be observed over time. This allows for an improvement of the signal to noise ratio similar to what is commonly done with data from AO-SLO instruments (c.f. Figs. 11 and 12). Furthermore the system can be used to study dynamic processes such as blood flow.

One benefit of the en-face OCT system has not yet been implemented into our system: the possibility of a dynamic focus. Since depth scanning is performed rather slowly, the focal plane can be shifted simultaneously with the coherence gate which results in a 3D volume of the retina with maintained high transverse resolution [36]. Our previous concept cannot be used for AO-imaging because it requires a change in the position of the last lens which would influence the wavefront measurement. However, with proper changes in the corresponding AO software, the deformable mirror itself can be used for shifting the focus dynamically.

Acknowledgments

Financial assistance from the Austrian Science Fund (FWF project P22329-N20) is gratefully acknowledged. The authors further acknowledge equipment support from W. Drexler (Medical University of Vienna) and fruitful discussions with R. J. Zawadzki (UC-Davis, Sacramento).